



**HAL**  
open science

## Parsimonious finite-volume frequency-domain method for 2D P-SV-wave modeling

R. Brossier, Jean Virieux, Stéphane Operto

► **To cite this version:**

R. Brossier, Jean Virieux, Stéphane Operto. Parsimonious finite-volume frequency-domain method for 2D P-SV-wave modeling. *Geophysical Journal International*, 2008, 175, pp.541-559. 10.1111/j.1365-246X.2008.03839.x . insu-00200052v1

**HAL Id: insu-00200052**

**<https://insu.hal.science/insu-00200052v1>**

Submitted on 20 Dec 2007 (v1), last revised 21 Sep 2009 (v2)

**HAL** is a multi-disciplinary open access archive for the deposit and dissemination of scientific research documents, whether they are published or not. The documents may come from teaching and research institutions in France or abroad, or from public or private research centers.

L'archive ouverte pluridisciplinaire **HAL**, est destinée au dépôt et à la diffusion de documents scientifiques de niveau recherche, publiés ou non, émanant des établissements d'enseignement et de recherche français ou étrangers, des laboratoires publics ou privés.

# **Parsimonious finite-volume frequency-domain method for 2D P-SV-wave modeling**

R. Brossier<sup>1</sup>, J. Virieux<sup>2</sup> and S. Operto<sup>3</sup>

<sup>1</sup> *Géosciences Azur, CNRS, IRD, UNSA, UPMC, Valbonne, France. E-mail: brossier@geoazur.unice.fr.*

*Ph/fax : +33492942662/+33492942610*

<sup>2</sup> *Laboratoire de Géophysique Interne et Tectonophysique, UJF, CNRS, Grenoble, France.*

*E-mail: Jean.Virieux@obs.ujf-grenoble.fr.*

<sup>3</sup> *Géosciences Azur, CNRS, IRD, UNSA, UPMC, Villefranche-sur-mer, France. E-mail: operto@geoazur.obs-vlfr.fr.*

Accepted date. Received date; in original form date

## **SUMMARY**

A new numerical technique for solving the 2D elastodynamic equations based on a finite-volume approach is proposed. The associated discretization is through triangles. Only fluxes of required quantities are shared between cells, relaxing meshing conditions compared to finite element methods. The free surface is described along the edges of the triangles which may have different slopes. By applying a parsimonious strategy, stress components are eliminated from the discrete equations and only velocities are left as unknowns in triangles, minimizing the core memory requirement of the simulation. Efficient PML absorbing conditions have been designed for damping waves around the grid. Since the technique is devoted to full waveform inversion, we implemented the method in the frequency domain using a direct solver, an efficient strategy for multiple-source simulations. Standard dispersion analysis in infinite homogeneous media shows that numerical dispersion is similar to those of  $O(\Delta x^2)$  staggered-grid finite-difference formulations when considering structured triangular meshes. The method is validated against analytical solutions of several canonical problems and with numerical solu-

tions computed with a well-established finite-difference time-domain method in heterogeneous media. In presence of a free surface, the finite-volume method requires ten triangles per wavelength for a flat topography and fifteen triangles per wavelength for more complex shapes, well below criteria required by the staircase approximation of finite-difference methods. Comparison between the frequency-domain finite-volume and the  $O(\Delta x^2)$  rotated finite-difference methods also shows that the former is faster and less-memory demanding for a given accuracy level. We developed an efficient method for 2-D P-SV-wave modeling on structured triangular meshes as a tool for frequency-domain full-waveform inversion. Further work is required to assess the method on unstructured meshes.

**Key words:** seismic wave propagation, numerical modeling, finite volume approach, elastic waves, frequency domain

## 1 INTRODUCTION

Seismic wave propagation has been investigated with various numerical methods such as finite-difference (FD), finite-element (FE) or boundary integral equations (BIE). The FD staggered-grid method proposed by Madariaga (1976) and Virieux (1986a) using the Yee scheme (Yee, 1966), based on the first-order velocity-stress hyperbolic system, is quite popular and have been intensively used in time domain for forward modeling as well as for seismic imaging. FE approaches have been recently designed with recent high-order interpolation leading to the spectral element method (Faccioli et al., 1997; Vilotte et al., 2005; Komatitsch and Vilotte, 1998; Chaljub et al., 2003). Other numerical methods have been developed such as Finite Volume approaches (FV) by Dormy and Tarantola (1995) with mitigated results and more recently by BenJemaa et al. (2007); Käser and Dumbser (2006) with promising perspectives.

Since the success of the full waveform inversion in the frequency domain (Pratt and Worthington, 1990; Pratt et al., 1996, 1998), applications to real data using the acoustic approximation have been performed for imaging complex structures (Ravaut et al., 2004; Operto et al., 2006) while reconstruction of elastic parameters is still a quite challenging problem (Gelis et al., 2007). An efficient method must be developed in the frequency domain for modeling elastic waves in heterogeneous

media with a free surface of arbitrary shape. This will allow to investigate elastic full-waveform inversion in realistic configurations. Aim of this paper is to present such a method.

FD methods require a high number of grid points per wavelength for minimal numerical dispersion especially nearby the free surface described by staircase approximation (Robertsson, 1996). Second-order-accurate rotated FD stencils allow to verify free surface conditions with a minimum of 25 nodes per shear wavelength for flat topography and 60 nodes per shear wavelength with complex topography (Saenger et al., 2000; Saenger and Bohlen, 2004; Bohlen and Saenger, 2006). Optimal FD stencils based on the mixed-grid method and anti-lumped mass have been designed for frequency-domain wave propagation modeling. This approach revealed very efficient for the acoustic wave equation (Jo et al., 1996; Hustedt et al., 2004) for which only 4 grid points per wavelength can be used but showed some limitations in the elastic case when a liquid-solid interface is involved in the simulation (Stekl and Pratt, 1998). In this case, only the abovementioned second-order rotated stencil can be used. Moreover, accuracy of the mixed-grid elastic stencil still requires further demonstration in the case of free surface with complex topography. The method we propose in this article will reduce the request of dense sampling nearby the free surface.

In this paper, we present a FV method based on the first-order hyperbolic elastodynamic system as usually done for FV formulations (Remaki, 1999). We shall deduce the discretized system of linear equations to be solved only for velocity components using the parsimonious strategy (Luo and Schuster, 1990). Numerical dispersion behaviour of this scheme will be analyzed before discussing the Perfectly Matched Layer (PML) conditions (Berenger, 1994). The implementation of the source will require specific attention before going to numerical validations both against analytical solutions and numerical solutions obtained by other numerical methods. For these examples, we may compare respective numerical costs of frequency-domain FD and FV methods. We shall conclude on potentialities of this FV approach in the frequency domain for the accurate modeling of seismic 2D P-SV waves and perspectives for inversion.

## 2 FINITE VOLUME FORMULATION

We consider first-order hyperbolic elastodynamic system for 2D P-SV waves in isotropic medium in the frequency domain where both velocities ( $V_x, V_z$ ) and stress ( $\sigma_{xx}, \sigma_{zz}, \sigma_{xz}$ ) are unknown quantities as described by the following differential system,

$$\begin{aligned}
-\iota\omega V_x &= \frac{1}{\rho(\mathbf{x})} \left\{ \frac{\partial \sigma_{xx}}{\partial x} + \frac{\partial \sigma_{xz}}{\partial z} \right\} + F_x \\
-\iota\omega V_z &= \frac{1}{\rho(\mathbf{x})} \left\{ \frac{\partial \sigma_{xz}}{\partial x} + \frac{\partial \sigma_{zz}}{\partial z} \right\} + F_z \\
-\iota\omega \sigma_{xx} &= (\lambda(\mathbf{x}) + 2\mu(\mathbf{x})) \frac{\partial V_x}{\partial x} + \lambda(\mathbf{x}) \frac{\partial V_z}{\partial z} - \iota\omega \sigma_{xx_0} \\
-\iota\omega \sigma_{zz} &= \lambda(\mathbf{x}) \frac{\partial V_x}{\partial x} + (\lambda(\mathbf{x}) + 2\mu(\mathbf{x})) \frac{\partial V_z}{\partial z} - \iota\omega \sigma_{zz_0} \\
-\iota\omega \sigma_{xz} &= \mu(\mathbf{x}) \left\{ \frac{\partial V_x}{\partial z} + \frac{\partial V_z}{\partial x} \right\} - \iota\omega \sigma_{xz_0},
\end{aligned} \tag{1}$$

where Lamé coefficients describing the medium are denoted by  $\lambda$ ,  $\mu$ , the density by  $\rho$  and the angular frequency by  $\omega$ . Source terms are either punctual forces ( $F_x, F_z$ ) or applied stresses ( $\sigma_{xx_0}, \sigma_{zz_0}, \sigma_{xz_0}$ ) as introduced in the system 1. The Fourier transform follows the usual convention as  $f(\omega) = \int_{-\infty}^{+\infty} f(t)e^{-\iota\omega t} dt$ . In order to develop pseudo-conservative formulation useful when we integrate over a surface in 2D, we shall consider the following new vector with three components  $\vec{T}^t = (T_1, T_2, T_3) = ((\sigma_{xx} + \sigma_{zz})/2, (\sigma_{xx} - \sigma_{zz})/2, \sigma_{xz})$ . Moreover, we must consider a finite domain and, therefore, we apply PML absorbing conditions (Berenger, 1994) through functions  $s_x, s_z$  for velocity equations and functions  $s'_x, s'_z$  for stress equations. More details on the expression of these damping functions  $s_x, s_z, s'_x, s'_z$  will be given later in the paper. The new differential system equivalent to the system 1 can be written as

$$\begin{aligned}
 -\omega\rho V_x &= s_x \frac{\partial(T_1 + T_2)}{\partial x} + s_z \frac{T_3}{\partial z} + \rho F_x \\
 -\omega\rho V_z &= s_x \frac{\partial T_3}{\partial x} + s_z \frac{\partial(T_1 - T_2)}{\partial z} + \rho F_z \\
 \frac{-\omega T_1}{\lambda + \mu} &= s'_x \frac{\partial V_x}{\partial x} + s'_z \frac{\partial V_z}{\partial z} - \frac{\omega T_1^0}{\lambda + \mu} \\
 \frac{-\omega T_2}{\mu} &= s'_x \frac{\partial V_x}{\partial x} - s'_z \frac{\partial V_z}{\partial z} - \frac{\omega T_2^0}{\mu} \\
 \frac{-\omega T_3}{\mu} &= s'_x \frac{\partial V_z}{\partial x} + s'_z \frac{\partial V_x}{\partial z} - \frac{\omega T_3^0}{\mu}
 \end{aligned} \tag{2}$$

We apply a surface integration over a control cell identified by the index  $i$ . For practical reasons of meshing, control cells are often taken as triangles or quadrangles but formulation still stands for any 2D shapes delimited by segments. Cell shape can be regular or irregular giving some flexibility in our medium geometrical description. Formulation presented here is based on triangle cells in a conformal mesh which imposes three edges and neighbours for each considered cell. We assume that quantities are constant inside each cell, assumption known as the  $P_0$  approximation. Higher-order interpolation  $P_k$  are often referred to discontinuous Galerkin methods (Käser and Dumbser, 2006). Thanks to the Green theorem, we end up with the discrete system written in a vectorial form (see Appendix A for a complete derivation)

$$\begin{aligned}
 -\omega A_i \rho_i \vec{V}_i &= \sum_{j \in \partial K_i} l_{ij} G_{ij} + A_i \rho_i \vec{F}_i \\
 -\omega A_i \Lambda_i \vec{T}_i &= \sum_{j \in \partial K_i} l_{ij} H_{ij} - \omega A_i \Lambda_i \vec{T}_i^0
 \end{aligned} \tag{3}$$

The surface of the  $i$  cell is denoted by  $A_i = \int_{K_i} dS$ . The index  $j \in \partial K_i$  labels the three neighbouring cells with a common edge with the  $i$  cell. The length of the edge between cells  $i$  and  $j$  is denoted by  $l_{ij}$ . Numerical approximation of fluxes is denoted by  $l_{ij} H_{ij}$  and  $l_{ij} G_{ij}$ . The matrix  $\Lambda_i$  is the diagonal matrix defined by  $\Lambda_i = \text{diag}(\frac{1}{\lambda_i + \mu_i}, \frac{1}{\mu_i}, \frac{1}{\mu_i})$ . Finally, source vectors applied inside the  $i$  cell is denoted by  $\vec{F}_i$  and  $\vec{T}_i^0$ .

Centred numerical fluxes of velocity and stress components between two cells, first proposed by

Remaki (1999) and used by BenJemaa et al. (2007) for elastodynamics in time-domain and Dolean et al. (2006) for Maxwell equations in frequency domain, are introduced because they preserve a discrete energy inside the entire zone away from PML. It gives us the following estimation of quantities  $G_{ij}$  and  $H_{ij}$ :

$$\begin{aligned} G_{ij} &= \sum_{r \in \{x,z\}} n_{ijr} N_k \frac{s_{r_i} \vec{T}_i + s_{r_j} \vec{T}_j}{2} \\ H_{ij} &= \sum_{r \in \{x,z\}} n_{ijr} M_k \frac{s'_{r_i} \vec{V}_i + s'_{r_j} \vec{V}_j}{2}, \end{aligned} \quad (4)$$

where the normal vector component  $r$  oriented for each edge of cell  $i$  towards cell  $j$  is denoted by  $n_{ijr}$ . Projector matrices defined for a vectorial formulation are denoted by  $M_k$  and  $N_k$ .

Geometrical properties of triangles give

$$\sum_{j \in \partial K_i} l_{ij} P_{ij} = 0 \quad (5)$$

where  $P_{ij} = \sum_{r \in \{x,z\}} n_{ijr}$ . This geometrical property ensures that, for first-order system, the unknowns in a given cell  $i$  depend only on the unknowns of the surrounding cells but not on the unknowns of the cell  $i$ , contributions cancelled by construction.

To minimize the number of unknowns, discrete equations expressing stress components, second vectorial equation of system 3, can be eliminated by inserting them into fluxes required in velocity equations, first vectorial equation of system 3, following the parsimonious strategy first proposed by Luo and Schuster (1990). After elimination of stress components, we end up with two algebraic

equations for the two unknown velocity components

$$\begin{aligned}
 \omega^2 V_{x_i} &= \omega F_{x_i} + \frac{\omega}{A_i \rho_i} \sum_{j \in \partial K_i} \frac{l_{ij}}{2} \left\{ n_{ijx} s_{x_j} \left[ \frac{\iota(\lambda_j + \mu_j)}{\omega A_j} \sum_{k \in \partial K_j} \frac{l_{jk}}{2} (n_{jkx} s'_{x_k} V_{x_k} + n_{jkz} s'_{z_k} V_{z_k}) + T_{1_j}^0 \right] \right. \\
 &+ n_{ijx} s_{x_j} \left[ \frac{\iota \mu_j}{\omega A_j} \sum_{k \in \partial K_j} \frac{l_{jk}}{2} (n_{jkx} s'_{x_k} V_{x_k} - n_{jkz} s'_{z_k} V_{z_k}) + T_{2_j}^0 \right] \\
 &\left. + n_{ijz} s_{z_j} \left[ \frac{\iota \mu_j}{\omega A_j} \sum_{k \in \partial K_j} \frac{l_{jk}}{2} (n_{jkx} s'_{x_k} V_{z_k} + n_{jkz} s'_{z_k} V_{x_k}) + T_{3_j}^0 \right] \right\} \\
 \omega^2 V_{z_i} &= \omega F_{z_i} + \frac{\omega}{A_i \rho_i} \sum_{j \in \partial K_i} \frac{l_{ij}}{2} \left\{ n_{ijz} s_{z_j} \left[ \frac{\iota(\lambda_j + \mu_j)}{\omega A_j} \sum_{k \in \partial K_j} \frac{l_{jk}}{2} (n_{jkx} s'_{x_k} V_{x_k} + n_{jkz} s'_{z_k} V_{z_k}) + T_{1_j}^0 \right] \right. \\
 &- n_{ijz} s_{z_j} \left[ \frac{\iota \mu_j}{\omega A_j} \sum_{k \in \partial K_j} \frac{l_{jk}}{2} (n_{jkx} s'_{x_k} V_{x_k} - n_{jkz} s'_{z_k} V_{z_k}) + T_{2_j}^0 \right] \\
 &\left. + n_{ijx} s_{x_j} \left[ \frac{\iota \mu_j}{\omega A_j} \sum_{k \in \partial K_j} \frac{l_{jk}}{2} (n_{jkx} s'_{x_k} V_{z_k} + n_{jkz} s'_{z_k} V_{x_k}) + T_{3_j}^0 \right] \right\}. \tag{6}
 \end{aligned}$$

where  $k \in \partial K_j$  labels the index of the cells  $j$ , neighbours of the cell  $i$ . Thanks to properties of triangle given by expression (5), thanks to centred flux estimations and to the parsimonious formulation leading to this algebraic system (6), velocity unknowns depend only on velocities of neighbours of neighbours of the cell: neighbouring velocity unknowns are not directly involved in the numerical scheme for a given element. Figure 1 illustrates this configuration on a regular mesh: the numerical scheme centred on the green central cell depends on the unknown at this cell and on the unknowns belonging to the neighbours of the neighbours cells (red cells). No dependency with blue-cell unknowns is observed as previously noticed by LeVeque (2007) as the black/red pattern of centred numerical schemes.

Equations 6 can be recast in matrix form as

$$\mathcal{A}V = \mathcal{B}$$

where the sparse impedance matrix  $\mathcal{A}$  contains 14 non-zero coefficients per row in the general case (i.e., without any regular structure) due to expected irregular numbering of cells inside the mesh. Let us underline that the corresponding matrix for the parsimonious rotated second-order FD stencil (Gelis et al., 2007) has eighteen non-zero elements.

Free surface condition is explicitly expressed in the numerical scheme by considering a ghost cell above the free surface with the same velocity and the opposite stress components than below the



free surface in order to guarantee continuity of displacements and normal stresses equal to zero respectively. Using these velocities and stresses in the ghost cell, stress flux across the free surface interface vanishes while the velocity flux is twice that which would have been obtained by neglecting the flux contribution above the free surface. This boundary condition was implemented by modifying accordingly the impedance matrix without introducing new unknown quantities.

### 3 NUMERICAL PROPERTIES

Discretization leads to numerical dispersion in the particle velocity wavefields. For unstructured meshes, the dispersion could not be estimated analytically while a regular distribution of equilateral triangles will allow such investigation. Moreover, we must consider specific properties at edges of the grid for extending the medium to infinity. Finally, the source implementation has to excite the entire grid by avoiding exciting a specific sub-grid related to the centred pattern of our system.

#### 3.1 Numerical dispersion analysis

One can estimate numerical dispersion of such discrete system for a regular distribution of equilateral triangles (see mesh configuration of the figure 1 for such pattern). We consider an incident plane wave propagating inside an infinite and homogeneous medium away from PML and source zones. The Hermitian structure of the matrix, thanks to the regular mesh, makes eigenvalues real. They are computed numerically for different Poisson ratios from 0 to 0.5, for different number of cells per wavelength and with incidence angles range between  $0^\circ$  and  $180^\circ$  with an interval of  $15^\circ$ . Dispersion curves are quite similar to those obtained by Virieux (1986b) using a  $2^{nd}$ -order accurate FD scheme as shown in figure 2. The rule of thumb of ten grid points per wavelength seems to provide acceptable propagation dispersion whatever is the value of shear wave velocity which can decrease to zero without any numerical instability. The rotated staggered-grid FD stencil gives similar results with a grid length higher by a factor of  $\sqrt{2}$  (Saenger et al., 2000). Let us remark

that we have considered the triangle edge length for the FV approach and the grid step length for the FD approach as our discrete reference values.

### 3.2 PML absorbing boundary conditions

The frequency domain allows a straightforward numerical implementation of PML conditions without any splitting of particle velocity components or additional integration of memory variables as for the time domain formulation thanks to a complex coordinate change (Chew and Liu, 1996). Numerical tests show that the PML efficiency depends strongly on the mesh structure in the PMLs. The PML absorbing boundary condition requires that the PML-PML interfaces are oriented along the Cartesian directions (Berenger, 1994). This condition is not verified if triangles of arbitrary orientations are used in the PML layers. In that case, we observed poor absorption as illustrated in Figure 4 (top panel) for a distribution of non constrained triangles in arbitrary orientations in the PML layers. Therefore, a constrained mesh in PML zones with multiple layers structure parallel to Cartesian directions (see the figure 3 for the discretization of the lower left quarter of the medium) provides efficient absorption of elastic waves. Of course, a transition is performed between main central zone of the grid and PML constrained zones. With this constraint on the mesh construction, at each parallel interface of PML layers, major part of energy is contained along the damped direction and numerical flux energy is globally damped by the variation of PML functions  $s_x, s_z, s'_x, s'_z$  as we move deeper inside the PML zone. We can remark that use of quadrangle cells, oriented along cartesian axes, in PML should provide a very efficient behaviour as absorbing boundaries but is less easier to implement with triangular mesh generators.

Standard frequency PML function is defined by

$$s_r = \frac{1}{1 + \nu\gamma_r/\omega}, \quad (7)$$

where the index  $r$  can be  $x$  or  $z$ . A similar expression is obtained for the  $s'_r$  function. Both functions are only used inside PML zones. Outside the damping zone, values of  $s_r$  and  $s'_r$  functions are simply equal to 1. The value  $\gamma_r$  is typically used as a polynomial or cosines function for a progressive energy damping. Numerical tests have shown a better behaviour by using a modified PML function derived from developments made by Drossaert and Giannopoulos (2007). The definition

of the damping functions  $s_r$  and  $s'_r$  are extended through the following equation

$$s_r = \frac{1}{\kappa_r + \nu\gamma_r/\omega}, \quad (8)$$

with expressions  $\kappa_r$  and  $\gamma_r$  as cosines functions. A linear dependency of term  $\gamma_r$  with frequency has shown a good damping behaviour for different range of frequencies. These functions are defined as

$$\begin{aligned} \gamma_r(l) &= \omega B \cos\left(\frac{l\pi}{2l_{pml}}\right) \\ \kappa_r(l) &= 1 + C \cos\left(\frac{l\pi}{2l_{pml}}\right), \end{aligned} \quad (9)$$

along the perpendicular direction with  $l_{pml}$  the size of PML zone which is taken as fifteen cells in examples we have selected in this article. An efficient damping has been obtained with values as  $B = 25$  and  $C = 2$  for equations 9. For an illustration of the PML mesh structure and of the numerical implementation of the wave absorbing effect, a test is performed in an homogeneous infinite medium with a P-wave velocity of  $2500 \text{ m/s}$  and a S-wave velocity of  $1558 \text{ m/s}$  and a density of  $1500 \text{ kg/m}^3$  inside a finite grid. The simulation is performed at  $4 \text{ Hz}$  with an unit explosive source. Figure 4 shows frequency map solution for non-constrained mesh (top) and constrained mesh (bottom). Only real part of horizontal velocity is shown but behaviour is similar for others components of solutions. Mesh structure has clearly a significant influence on the PML efficiency.

### 3.3 Source implementation

Introduction of both punctual forces and punctual excitation stresses in the first-order system 1 allows us to develop various punctual excitations: an impulsive force along cartesian directions or an explosive source could be easily applied using forces and stresses respectively. A staggered behaviour over the mesh occurs in discrete equations where one cell unknown does not depend directly from its neighbours unknowns but from the neighbour unknowns of the neighbour cells. For particular mesh configurations as regular equilateral mesh, if the source excitation is applied on one cell, simulations show that only one cell out of two is excited in the mesh. For avoiding this check-board pattern, we spread the source over several cells using a Gaussian function. Of course,

the numerical dispersion will express its properties based on twice the coarseness of the grid: this is the price to be paid when considering centred fluxes. A similar observation could be done for the rotated FD scheme. It has been the main reason for moving to the staggered grid formulation by different authors. The figure 5 shows this pattern for an infinite homogeneous model with a central horizontal force. A single cell is excited on the left figure whereas a gaussian source is applied on 29 cells on the right. We can also notice that, for the model with free surface, explicit formulation of such boundary recouples the two decoupled submeshes as shown on the figure 6 with the same source configuration as the previous test. We still need to implement a smooth source excitation for propagation inside the medium.

#### 4 NUMERICAL RESULTS

Several benchmarks will be presented for assessing the accuracy of this new method and we shall focus more specifically on the influence of the mesh structure. Indeed, numerical tests in regular equilateral meshes and arbitrary unstructured meshes have shown the influence of mesh regularity on solution accuracy: in spite of mesh refining, results do not converge to true solutions when considering unstructured meshes whereas no problem occurs with regular meshes. A sensitivity study on perturbed regular meshes has confirmed this behaviour. Accuracy problems in unstructured meshes are typically travel time shifts in seismograms. Dolean et al. (2006) have observed the same behaviour of convergence dependency for  $P_0$  interpolation when applied to Maxwell equations in frequency domain while convergence of linear  $P_1$  interpolation seems to be less dependent of mesh regularity. Moreover, the theoretical evaluation of the  $2^{nd}$ -order accuracy in space of the numerical scheme was demonstrated for regular structured meshes Remaki (1999). We shall specify in our different comparisons when we consider regular equilateral meshes or unstructured meshes. In the following, we first compare FV results with analytical solutions for different canonical problems. Solutions in more complex models are then compared with FD solutions.

Analytical solutions and reference FD codes have been constructed in the time domain and comparisons will be performed in this domain. Of course, FV solutions are computed for several frequencies spanning over the source wavelet bandwidth. For avoiding the wrap-around effect in

seismograms, complex frequencies (Mallick and Frazer, 1987) are used in frequency domain simulations. An inverse Fast Fourier Transform will give us seismograms in the time domain for the comparison of solutions. Size of the cells will be chosen with respect to maximal frequency of the source bandwidth. Results in unstructured meshes are finally illustrated.

## 4.1 Comparison with analytical solutions

### 4.1.1 *Infinite homogeneous model with explosive source : acoustic case*

Acoustic propagation can be modeled inside an infinite homogeneous elastic medium by using an explosive source which generates only a P-wave pulse. The numerical grid is bounded by four absorbing layers on edges. For the homogeneous case, analytical solutions are build up for the Helmholtz equation. A comparison of radial velocity with analytical solution is performed for a 2500  $m/s$  P-wave velocity medium with a regular equilateral mesh of size 1/10 of P-wavelength (no S-wave generated). Figure 7 shows the seismogram of radial velocity at a receiver at a distance of 500  $m$  from the source and shows the good agreement between FV (crosses) and analytical (continuous line) seismograms. Tangential velocity is not strictly equal to zero due to smooth source and numerical errors but still remains negligible.

### 4.1.2 *Flat free surface medium : Garvin problem*

Garvin analytical solution deals with propagation of elastic waves in an homogeneous half space with flat free surface and an explosive source (Garvin, 1956). Comparison with Garvin solution is a quite challenging problem because FV method must model Rayleigh waves with good accuracy nearby the free surface, a critical issue for efficient full waveform inversion algorithm. An homogeneous medium with a P-wave velocity of 3464  $m/s$ , a S-wave velocity of 2000  $m/s$  and a density of 2000  $kg/m^3$  of density is considered. A gaussian explosive source is taken at 150  $m$  depth with 15  $m$  of correlation length and a line of receivers is set on the surface from offset 200  $m$  to 4000  $m$  with a space step of 200  $m$ . A Ricker wavelet of central frequency 4  $Hz$  is chosen. Simulation is performed over the source bandwidth ranging from 0  $Hz$  to 14  $Hz$ . Regular equilateral mesh is taken with a cell edge size of 15  $m$  which represents 1/10 of S-wavelength.

Horizontal and vertical particle-velocity seismograms computed with the FV method are compared with analytical ones in Figure 8. Direct and Rayleigh waves are both accurately modeled in shape and amplitude for the whole range of offsets for the two components. No time shift appears with offset which confirms the small dispersion of the scheme when considering 10 cells per S-wavelength.

#### *4.1.3 Two layers model with horizontal interface*

An analytical solution can be constructed when considering two homogeneous half spaces. A compressional point source will act in the upper layer. A software code, named EX2DELEL and provided by the Spice consortium (<http://www.spice-rtn.org>) was used to compute these solutions. Green's functions are first computed by Cagniard-De Hoop technique and a numerical convolution with the source wavelet gives the total response. FV simulation is performed with PML conditions on the four edges of the model for considering an infinite medium. The model dimensions are  $12 \times 2.5 \text{ km}$ . The interface between the two layers is at a depth of  $1150 \text{ m}$ . Receivers are placed on a line at a depth of  $280 \text{ m}$  with a space step of  $200 \text{ m}$  from  $0 \text{ m}$  to  $12000 \text{ m}$  of distance, leading to an array of 201 sensors. Explosive source is placed at a distance of  $500 \text{ m}$  and a depth of  $370 \text{ m}$  with a correlation length of  $30 \text{ m}$ . The source wavelet is a Ricker wavelet with a central frequency of  $4 \text{ Hz}$ . Two tests are performed in regular equilateral meshes to evaluate liquid/solid and solid/solid interfaces.

#### **Liquid-solid interface**

Liquid-solid interfaces modeling is quite challenging for marine acquisition or simulation with fluid reservoir as discontinuities must exist at the boundary. Because of these discontinuities, we must design an explicit interface condition following the same strategy as described by BenJemaa et al. (2007) for fault simulations: we modify the impedance matrix for both cells sharing this interface in order to allow discontinuities of tangential velocities on the interface. Upper medium has been considered as an acoustic one with a P-wave velocity of  $1500 \text{ m/s}$ , a S-wave velocity of  $0 \text{ m/s}$  and a density of  $1000 \text{ kg/m}^3$  while the lower medium has a P-wave velocity of  $3400 \text{ m/s}$ , a S-wave velocity of  $1963 \text{ m/s}$  and a density of  $2400 \text{ kg/m}^3$ . A discretization of 13

cells per P-wavelength in the acoustic domain has been chosen for keeping the numerical dispersion negligible. Figure 9 shows the horizontal and vertical components of particle velocity for the analytical (discontinuous red), FV (continuous black) and residual (discontinuous blue) solutions. A good agreement between analytical and FV solutions is observed. However, we can see parasite reflections from PML zones exactly where the acoustic/elastic interface penetrates the PML layer. Figure 10 illustrates such reflections for a shorter model in offset.

### **Solid-solid interface**

Solid-solid interface test is performed with values of 2500  $m/s$ , 1558  $m/s$  and  $1500kg/m^3$  for P-wave velocity, S-wave velocity and density for the upper half-space and values of 3400  $m/s$ , 1963  $m/s$  and  $2400kg/m^3$  respectively for the lower half-space. The FV seismograms were computed in a regular mesh with ten cells per shear wavelength. A good agreement is observed between analytical and FV seismograms (Figure 11). Note the efficient absorption of the PML in the case of the elastic/elastic interface.

## **4.2 Comparison with numerical solutions**

FV method needs to be benchmarked with other numerical techniques applied to more complex medium, which should be more representative of realistic applications of full waveform inversion. The FV solutions are validated against seismograms computed with a time-domain  $O(\Delta x^2)$  rotated staggered-grid FD method (Saenger et al., 2000) for three complex media: the Corner-Edge model, an homogeneous hill model for considering complex topography and a realistic heterogeneous model corresponding to a subset of the so called Marmousi II model.

### *4.2.1 Corner-Edge Model*

A synthetic model, named the Corner-Edge model (Figure 12), is defined by a flat free surface and a corner with sharp velocity contrast which introduces multiple reflections and diffractions for both body and surface waves (Virieux, 1986a). The upper medium has a P-wave velocity of 6000  $m/s$  while the lower medium a P-wave velocity of 9000  $m/s$ . The S-wave velocity is computed from the P-wave velocity with a ratio of  $\sqrt{3}$ . The model has a homogeneous density of 2500  $kg/m^3$ .

The explosive source located at ( $x=7500\text{ m}$ ,  $z=2900\text{ m}$ ) and it has a Ricker wavelet of central frequency  $4\text{ Hz}$  as the time function. Receiver line is placed below the topography at a depth of  $30\text{ m}$  with a receiver spacing of  $50\text{ m}$  from  $0\text{ m}$  to  $18000\text{ m}$ . An equilateral mesh is constructed with an edge length of  $26.6\text{ m}$  corresponding to a discretization rule of ten cells per minimum shear wavelength. Agreement between the FD and FV solutions is illustrated in Figure 13.

#### 4.2.2 *Complex topography Model*

An homogeneous model with a hill-shaped topography is used for assessing the accuracy of the FV method with non-flat free surface. An homogeneous ( $4000\text{ m/s}$  and  $2309\text{ m/s}$  for P-wave and S-wave velocities respectively,  $2000\text{ kg/m}^3$  for density) medium is used. An explosive source is set in the middle of the hill,  $25\text{ m}$  below the topography and it has a Ricker wavelet of central frequency  $4\text{ Hz}$  as a time dependence. Receiver line is located at depth of  $5\text{ m}$  below the free surface. Figure 14 shows the real part of a 10-Hz monochromatic wavefield for the horizontal velocity component. Equilateral mesh allows to model topography by straight lines (figure 15) without the stair-case description of FD methods. This description is not perfect as it should be with an unstructured mesh, but the numerical simulations have shown quite accurate results with 15 cells per shear wavelength with such topography whereas  $2^{nd}$ -order rotated staggered-grid FD stencil requires more than 60 points. The FV and FD seismograms computed with the two above-mentioned discretization rules (15 and 60 cells per shear-wavelength respectively) are compared in figure 16 showing a good agreement. Surface waves are well modeled and no numerical dispersion occurs. Simulations with a finer meshes led to comparable seismograms for both the FV and FD methods.

#### 4.2.3 *Realistic model: a subset of the Marmousi II model*

Marmousi II synthetic model represents a complex elastic medium which makes it suitable for testing the FV method we propose. A limited target of the model with multiple interfaces was chosen in order to limit core memory requested by the frequency-domain formulation used for building time-domain seismograms. This target, whose dimensions are  $5000\text{ m} \times 2000\text{ m}$  ( $6000\text{ m}$



x 2500 m with PML layers), is illustrated in the figure 17 for P-Wave velocities. An explosive source is located at ( $x=1000$  m,  $z=100$  m) and a Ricker wavelet of central frequency 4 Hz is considered. Receiver line is set at a depth of 25 m below the topography. Edges of the regular triangular mesh have a length of 7.1 m corresponding to 10 cells per shear wavelength. Figure 18 gives seismograms at receivers. Comparison with the FD method shows quite similar results. Small differences occur for horizontal velocity and could be attributed to the model description which is slightly different for the square and the triangle parameterization. FV simulations in finer triangular meshes led to similar seismograms hence, providing an additional validation of the discretization rule of ten cells per S-wavelength for heterogeneous media which is quite encouraging for future work.

### 4.3 Numerical tests with unstructured meshes

FV method is now analyzed in unstructured meshes. The  $P_0$  interpolation should provide solutions with a given level of accuracy in such meshes. Previous hill model and Marmousi II model will be considered. The FV solutions computed in equilateral mesh will be used as reference solutions. Unstructured meshes allow to model very precisely the free surface when complex topography is considered. No constraints on triangle angles have been applied for both models. Moreover, triangles sizes can be locally adapted to the propagated wavelengths to minimize the number of cells and, therefore, the number of unknowns in the linear system to be solved, a very appealing feature when performing the factorization of the impedance matrix. The Hill model simulation is performed with an unstructured mesh by considering the discretization rule of fifteen cells per minimum shear wavelength. Comparison between seismograms computed in equilateral structured and unstructured meshes is shown in Figure 19. One can note a good match of the amplitudes whereas a travelttime advance increasing with propagation time is observed in the seismograms computed in the unstructured mesh. The Marmousi II model simulation was performed in an unstructured mesh adapted to the local shear-wave velocity with at least ten cells per shear wavelength. Seismograms look like similar to those computed in equilateral mesh (compare Figures 18 and 20). However, direct comparison between the seismograms computed in the equilateral and unstructured meshes

shows a kinematic mismatch similar to that observed for the hill model, that is an advance of the seismograms computed in unstructured meshes increasing with propagation time. Simulations in finer unstructured meshes for the hill and Marmousi II models didn't improve the kinematic accuracy of the simulations. We conclude that the  $P_0$  interpolation prevents convergence behaviour whatever is the mesh size when considering unstructured meshes as already underlined.

## 5 NUMERICAL COST OF METHOD

The computational cost of the FV method is presented for the target of the Marmousi II model introduced in the previous section (Figure 17). The source is an explosion. The modeled frequency is 13 Hz. We compare the CPU time and memory requirement of the FV method with the 2<sup>nd</sup>-order parsimonious rotated frequency-domain FD method (Gelis et al., 2007). Both methods make use of the direct solver MUMPS (MUMPS-team, 2007) which performs the resolution of the linear system by a LU decomposition of the sparse matrix by a multifrontal approach. The medium is discretized with 10 cells per minimum S-wavelength for the FV approach in regular equilateral mesh, with 10 cells per local S-wavelength for the FV method in unstructured mesh and with 28 points for the FD method in order to have an acceptable numerical dispersion.

Table 1 illustrates requirements of both methods for a sequential execution on a single processor. The coarser parameterization of the FV naturally leads to less unknowns to be computed and a less expensive estimation in terms of CPU time and core memory for all MUMPS phases: a factor of 2.5 can be noticed for this example between FV in regular mesh and FD. Moreover, adaptive unstructured mesh allows to significantly decrease numerical resources when heterogeneous medium are considered. However, mesh description of medium introduces several additional tables build-up and manipulation for matrix construction which are more time consuming than the simple implicit construction of FD techniques on regular grid. Extra CPU time cost of FV methods, although small for the different MUMPS numerical procedures, shall occur only once when considering a full waveform inversion algorithm and will not hamper the benefit of using a coarser grid for the FV method.

## 6 DISCUSSION AND CONCLUSION

A FV method has been formulated in the space-frequency domain for 2D P-SV wave propagation. By using the parsimonious approach, only velocity quantities are used in the build-up of the impedance matrix. Comparisons of numerical solutions with analytic and numerical reference solutions in canonical and realistic configurations have shown that structured equilateral mesh gives accurate results for a discretization of 10 cell per shear wavelength even if topography and surface waves are considered. Complex topography should require finer description of 15 cells, coarser than classical FD due to triangular meshing. Unstructured meshes are easily taken into account in formulation but suffers from a lack of kinematic accuracy even if fine meshes are considered. CPU/memory requirements are naturally less expensive than FD in spite of complex table manipulations due to the mesh description of medium. Finally, FV method in regular meshes appears to be very efficient when compared with FD methods especially when realistic topography is considered. Considering unstructured meshes allows a significant decrease of numerical resources in spite of weaker accuracy of the wavefield estimation. Future work will focus on the requested accuracy in the forward modeling for the application of full waveform inversion. We may investigate the usefulness of unstructured meshes and the correlated accuracy for such imaging strategy. As an alternative, moving to higher order for the interpolation in the discontinuous Galerkin approach will be a possibility. By considering the  $P_1$  interpolation, we may provide a good compromise between accuracy for the wavefield estimation and the efficiency required for the inversion.

## ACKNOWLEDGMENTS

This research was funded by the SEISCOPE consortium (<http://geoazur.unice.fr/SEISCOPE>) sponsored by BP, CGG-VERITAS, EXXON-MOBIL, SHELL and TOTAL. LU factorization of impedance matrix is performed with package MUMPS (MUMPS-team, 2007) available on <http://graal.ens-lyon.fr/MUMPS/index.html>. Mesh generation is performed with help of TRIANGLE (Shewchuk (1996)), available on <http://www.cs.cmu.edu/~quake/triangle.html>. Garvin's problem analytical solutions have been computed with code provided by U. Iturrarán and F. J. Sánchez-Sesma. Two layers analytic solution have been computed with EX2DELEL code,

available on <http://www.spice-rtn.org/library/software/EX2DELEL>. Many thanks to Mondher Ben Jemaa, Nathalie Glinsky, Stéphane Lanteri, Serge Piperno of the project CAIMAN for interesting and stimulating discussions on the DG Pk approach. Access to the high performance computing facilities of MESOCENTRE SIGAMM computer center provided the required computer resources and we gratefully acknowledge both this facility and the support of the staff, in particular A. Miniussi.

## References

- BenJemaa, M., Glinsky-Olivier, N., Cruz-Atienza, V. M., Virieur, J., and Piperno, S. (2007). Dynamic non-planar crack rupture by a finite volume method. *Geophysical Journal International*, 171:271–285.
- Berenger, J.-P. (1994). A perfectly matched layer for absorption of electromagnetic waves. *Journal of Computational Physics*, 114:185–200.
- Bohlen, T. and Saenger, E. H. (2006). Accuracy of heterogeneous staggered-grid finite-difference modeling of rayleigh waves. *Geophysics*, 71:109–115.
- Chaljub, E., Capdeville, Y., and Vilotte, J. (2003). Solving elastodynamics in a fluid-solid heterogeneous sphere: a parallel spectral element approximation on non-conforming grids. *J. Compu. Phys.*, 187:457–491.
- Chew, W. C. and Liu, Q. H. (1996). Perfectly matched layers for elastodynamics: a new absorbing boundary condition. *J. Compu. Acous.*, 4:341–359.
- Dolean, V., Fol, H., Lanteri, S., and Piperno, S. (2006). Méthode de type galerkin discontinu pour la résolution numérique des équations de maxwell en régime fréquentiel. Rapport de Recherche 5904, INRIA Sophia-Antipolis.
- Dormy, E. and Tarantola, A. (1995). Numerical simulation of elastic wave propagation using a finite volume method. *Journal of Geophysical Research*, 100:2123–2133.
- Drossaert, F. H. and Giannopoulos, A. (2007). A nonsplit complex frequency-shifted PML based on recursive integration for FDTD modeling of elastic waves. *Geophysics*, 72(2):T9–T17.

- Faccioli, E. F., Paolucci, R., and Quarteroni, A. (1997). 2D and 3D elastic wave propagation by a pseudo-spectral domain decomposition method. *J. Seismol.*, 1:237–251.
- Garvin, W. W. (1956). Exact transient solution of the buried line source problem. *Proc. Roy. Soc. London*, 234:528–541.
- Gelis, C., Virieux, J., and Grandjean, G. (2007). 2D elastic waveform inversion using born and rytov approximations in the frequency domain. *Geophys. J. Int.*, 168:605–633.
- Hustedt, B., Operto, S., and Virieux, J. (2004). Mixed-grid and staggered-grid finite difference methods for frequency domain acoustic wave modelling. *Geophysical Journal International*, 157:1269–1296.
- Jo, C. H., Shin, C., and Suh, J. H. (1996). An optimal 9-point, finite-difference, frequency-space 2D scalar extrapolator. *Geophysics*, 61:529–537.
- Käser, M. and Dumbser, M. (2006). An Arbitrary High Order Discontinuous Galerkin Method for Elastic Waves on Unstructured Meshes I: The Two-Dimensional Isotropic Case with External Source Terms. *Geophysical Journal International*, 166:855–877.
- Komatitsch, D. and Vilotte, J. P. (1998). The spectral element method: an efficient tool to simulate the seismic response of 2D and 3D geological structures. *Bull. Seismol. Soc. Am.*, 88:368–392.
- LeVeque, R. J. (2007). *Finite Difference Methods for Ordinary and Partial Differential Equations, Steady State and Time Dependent Problems*. SIAM.
- Luo, Y. and Schuster, G. T. (1990). Parsimonious staggered grid finite-differencing of the wave equation. *Geophysical Research Letters*, 17(2):155–158.
- Madariaga, R. (1976). Dynamics of an expanding circular fault. *Bull. Seismol. Soc. Am.*, 66:639–666.
- Mallick, S. and Frazer, L. N. (1987). Practical aspects of reflectivity modeling. *Geophysics*, 52:1355–1364.
- MUMPS-team (2007). *MUMPS - MULTifrontal Massively Parallel Solver users' guide - version 4.7 (April 2007)*. ENSEEIHT-ENS Lyon, <http://www.enseeiht.fr/apo/MUMPS/> or <http://graal.ens-lyon.fr/MUMPS>.
- Operto, S., Virieux, J., Dessa, J. X., and Pascal, G. (2006). Crustal imaging from

- multifold ocean bottom seismometers data by frequency-domain full-waveform tomography: application to the eastern nankai trough. *Journal of Geophysical Research*, 111(B09306):doi:10.1029/2005JB003835.
- Pratt, R. G., Shin, C., and Hicks, G. J. (1998). Gauss-newton and full newton methods in frequency-space seismic waveform inversion. *Geophysical Journal International*, 133:341–362.
- Pratt, R. G., Song, Z. M., and Warner, M. (1996). Two-dimensional velocity models from wide-angle seismic data by wavefield inversion. *Geophys. J. Int.*, 124:323–340.
- Pratt, R. G. and Worthington, M. H. (1990). Inverse theory applied to multi-source cross-hole tomography. Part 1: acoustic wave-equation method. *Geophysical Prospecting*, 38:287–310.
- Ravaut, C., Operto, S., Improta, L., Virieux, J., Herrero, A., and dell’Aversana, P. (2004). Multi-scale imaging of complex structures from multi-fold wide-aperture seismic data by frequency-domain full-wavefield inversions: application to a thrust belt. *Geophysical Journal International*, 159:1032–1056.
- Remaki, M. (1999). A new finite volume scheme for solving maxwell’s system. *COMPEL*, 19(3):913–931.
- Robertsson, J. O. A. (1996). A numerical free-surface condition for elastic/viscoelastic finite-difference modeling in the presence of topography. *Geophysics*, 61:1921–1934.
- Saenger, E. H. and Bohlen, T. (2004). Finite-difference modelling of viscoelastic and anisotropic wave propagation using the rotated staggered grid. *Geophysics*, 69:583–591.
- Saenger, E. H., Gold, N., and Shapiro, S. A. (2000). Modeling the propagation of elastic waves using a modified finite-difference grid. *Wave motion*, 31:77–92.
- Shewchuk, J. R. (1996). Triangle: Engineering a 2D Quality Mesh Generator and Delaunay Triangulator. In Lin, M. C. and Manocha, D., editors, *Applied Computational Geometry: Towards Geometric Engineering*, volume 1148 of *Lecture Notes in Computer Science*, pages 203–222. Springer-Verlag. From the First ACM Workshop on Applied Computational Geometry.
- Stekl, I. and Pratt, R. G. (1998). Accurate viscoelastic modeling by frequency-domain finite difference using rotated operators. *Geophysics*, 63:1779–1794.

Vilotte, J., Festa, G., and Madariaga, R. (2005). Spectral element simulations of rupture dynamics along kinked faults. In *EOS Transactions*, volume 86. American Geophysical Union, San Francisco, USA.

Virieux, J. (1986a). P-SV wave propagation in heterogeneous media, velocity-stress finite difference method. *Geophysics*, 51:889–901.

Virieux, J. (1986b). *Séismes: rupture et onde (volumes I et II)*. PhD thesis, Université Paris VII.

Yee, K. S. (1966). Numerical solution of initial boundary value problems involving maxwell's equations in isotropic media. *IEEE Trans. Antennas and Propagation*, 14:302–307.

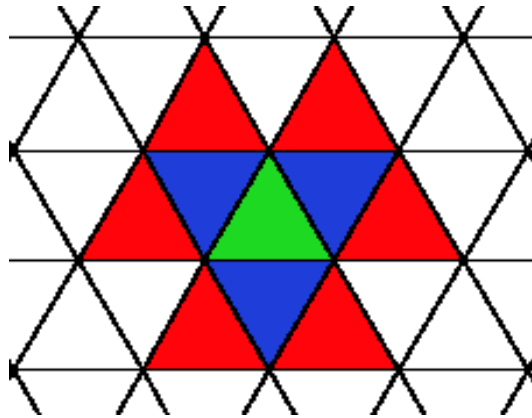


**Figure 1.** *Illustration of numerical scheme. In green, the central cell where the numerical scheme is built. In blue, its neighbour cells whose unknowns do not influence the scheme. In red, the neighbours of the neighbours cells whose unknowns are involved in the scheme.*



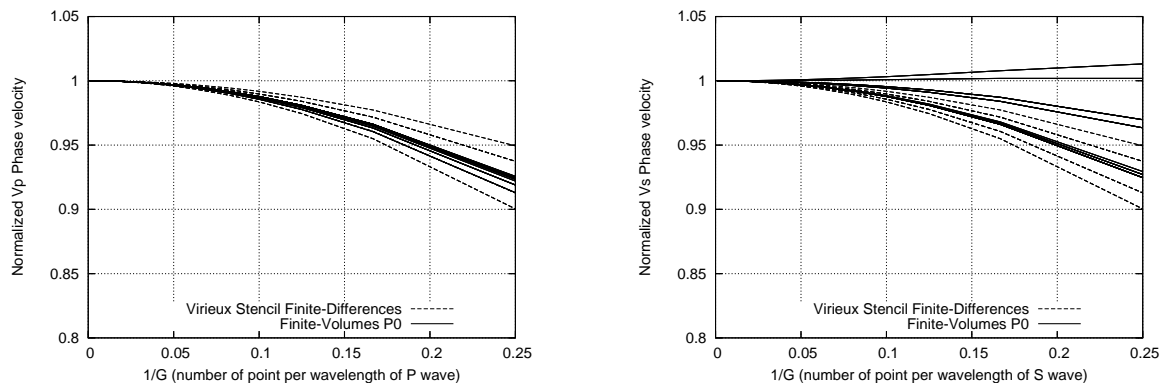


**Figure 2.** *P*-wave (right) and *S*-wave (left) normalized phase-velocity dispersion curves for different plane waves with various incident angles for both the FV (continuous) and the FD approaches (discontinuous).

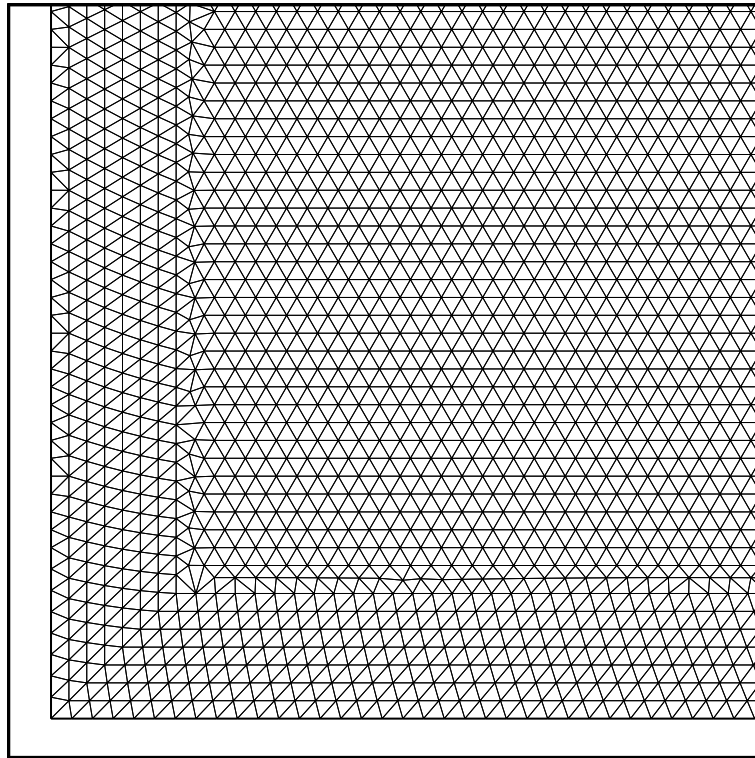


**Figure 3.** *PML construction with multiple layers structure parallel to Cartesian directions for the lower left quarter of the medium.*

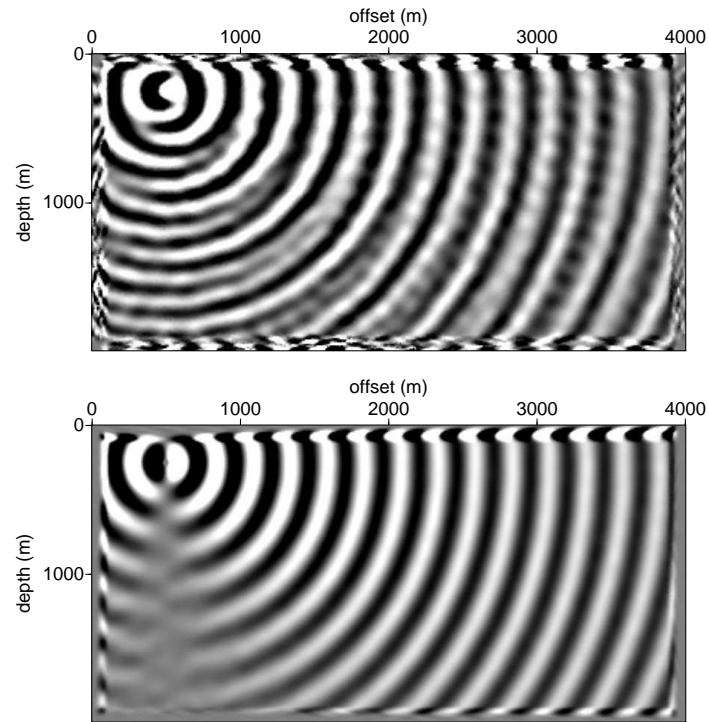


**Figure 4.** *Frequency map solutions where the real part of horizontal velocity for different PML configuration is displayed. No mesh constraints are applied on top panel whereas mesh constraints are applied in bottom respectively*

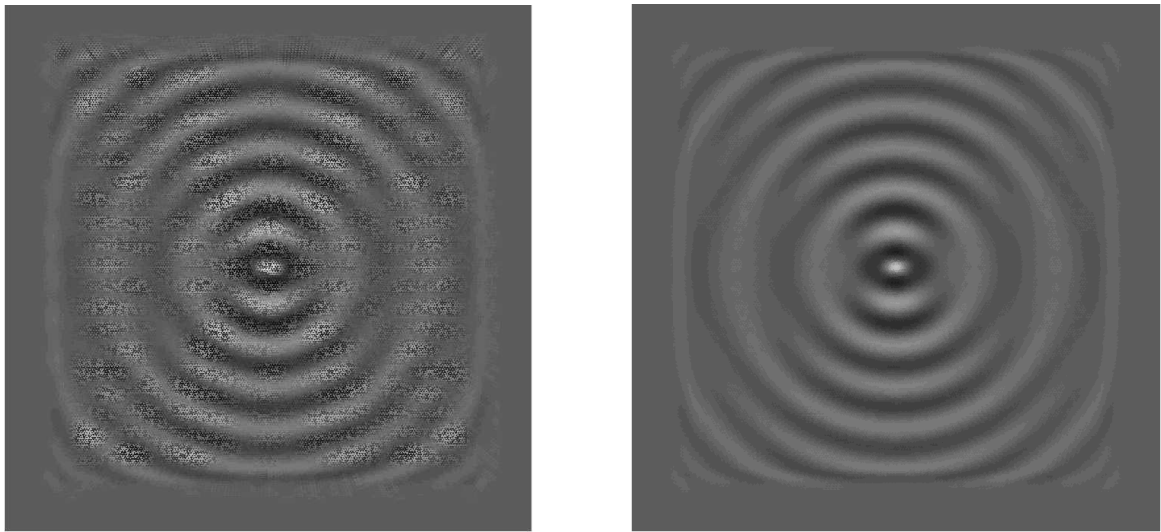


**Figure 5.** *Frequency map solutions with the real part of the horizontal velocity for a horizontal punctual force in infinite medium. A single cell excitation is shown on left and a smooth source excitation on several cells (29) is shown on the right.*

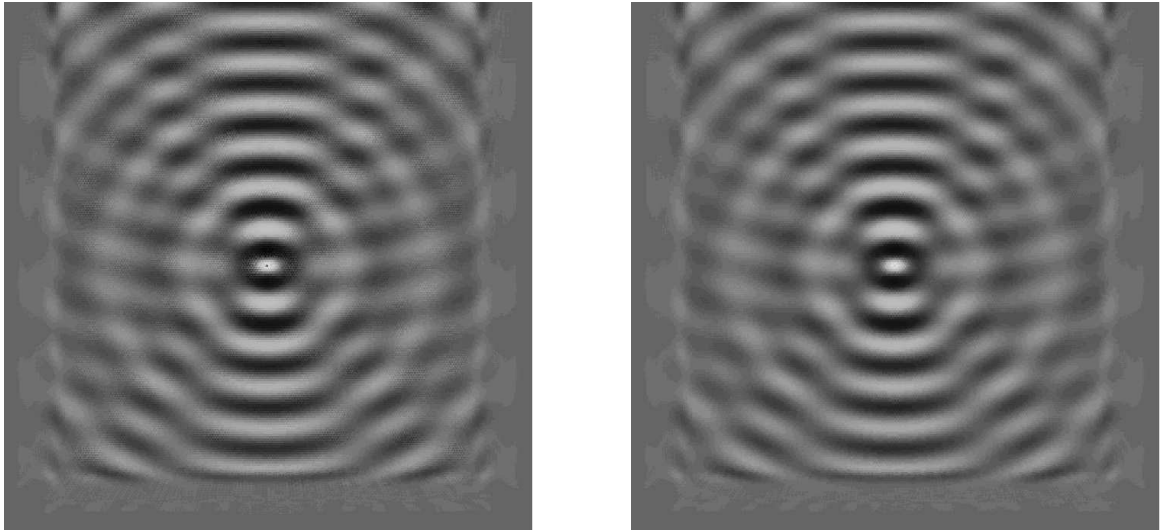


**Figure 6.** *Frequency map solutions, real part of horizontal velocity for horizontal punctual force in a flat topography model. A single cell excitation is shown on left and a smooth source excitation on several cells (29) is shown on right. Mesh pattern is less visible than for the figure 5 but is still present on the left panel.*

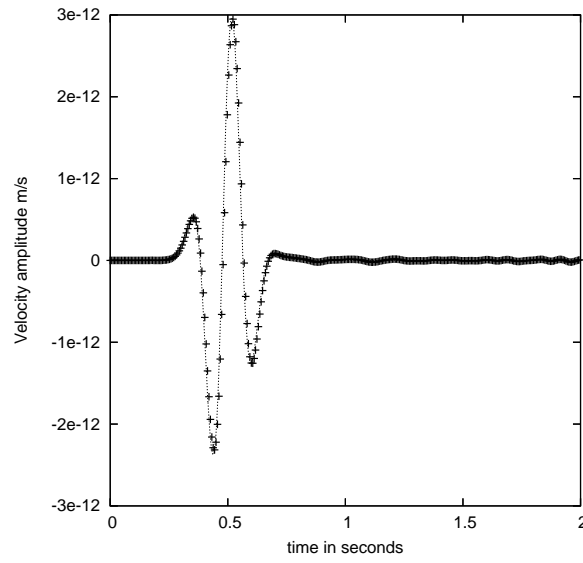


**Figure 7.** Comparison between analytical (continuous line) and numerical (crosses) seismograms for acoustic case

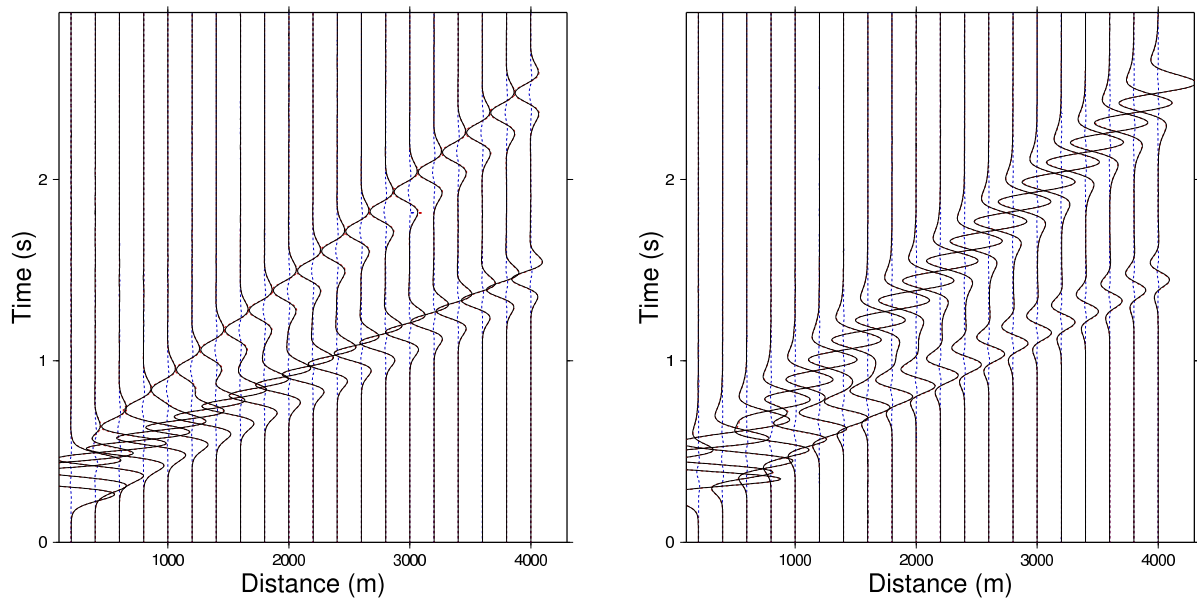


**Figure 8.** *Seismograms for the Garvin problem. Horizontal and vertical components of velocity at receivers are shown on the left and on the right respectively. Analytical solution is represented by discontinuous red lines, FV by continuous black lines and differences by discontinuous blue lines.*

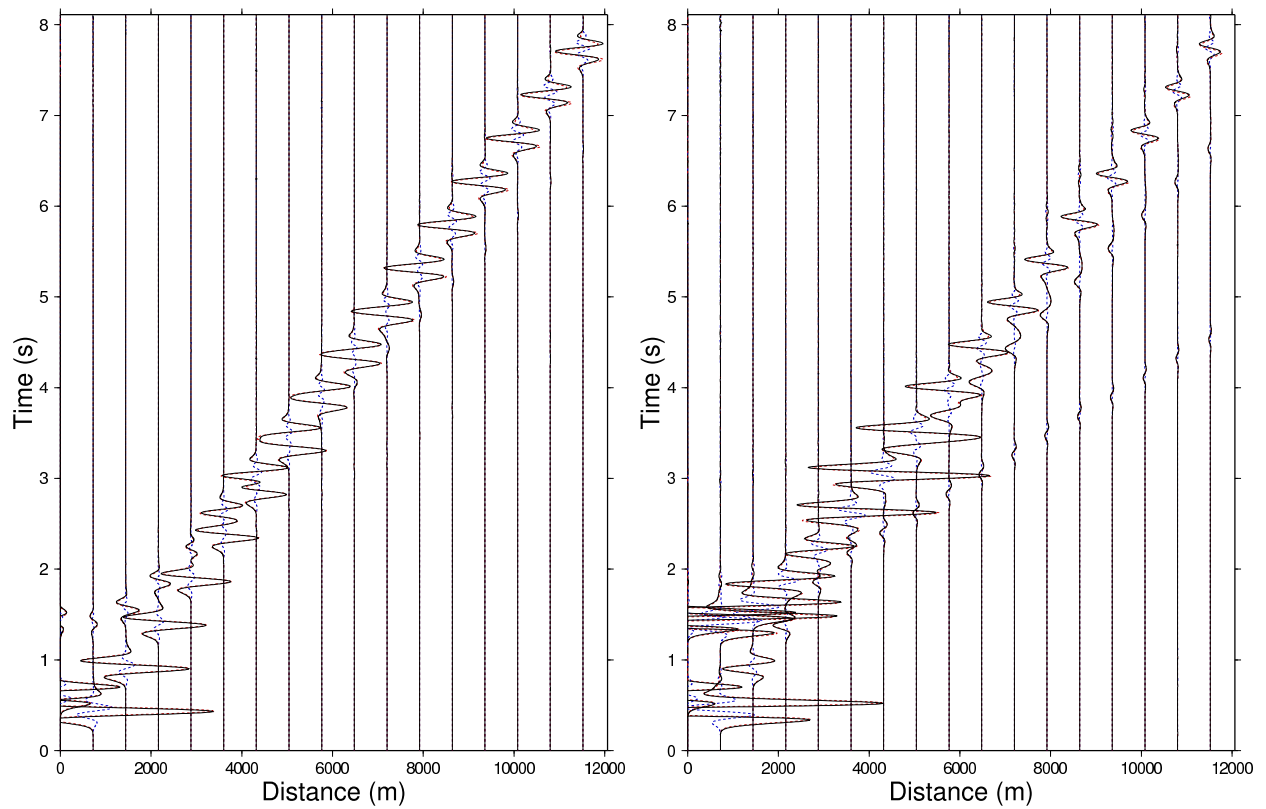


**Figure 9.** Seismograms computed in the two-layer model with liquid-solid interface. Horizontal and vertical components of velocity at receivers are shown on the left and on the right respectively. Analytical solution is represented by discontinuous red lines, FV by continuous black lines and residuals by discontinuous blue lines.



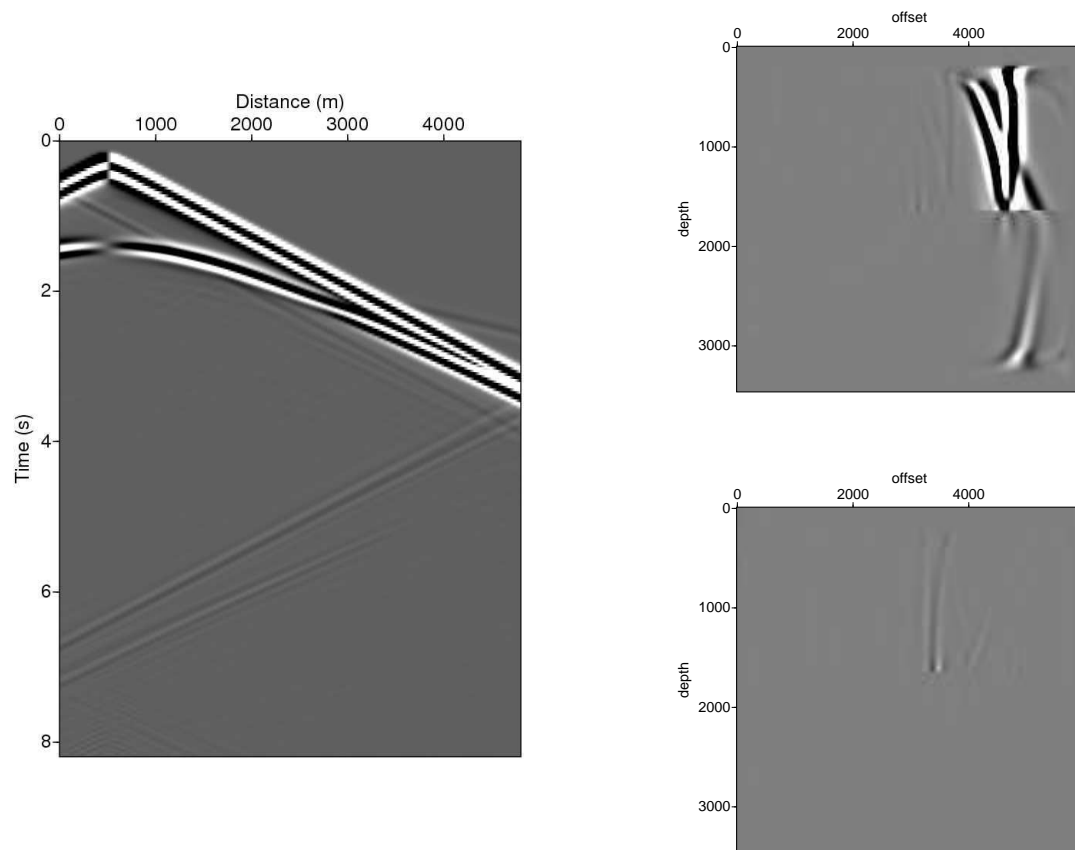


**Figure 10.** Seismograms at receivers positions (left) and snapshots (right) for horizontal components of velocities for two layers problem with liquid-solid interface and short offset geometry. Note parasite reflexions from the PML in the case of liquid-solid interface. The top snapshot illustrates incident wavefield at 2.8 s and the bottom one shows reflected waves from PML at 4.8 s

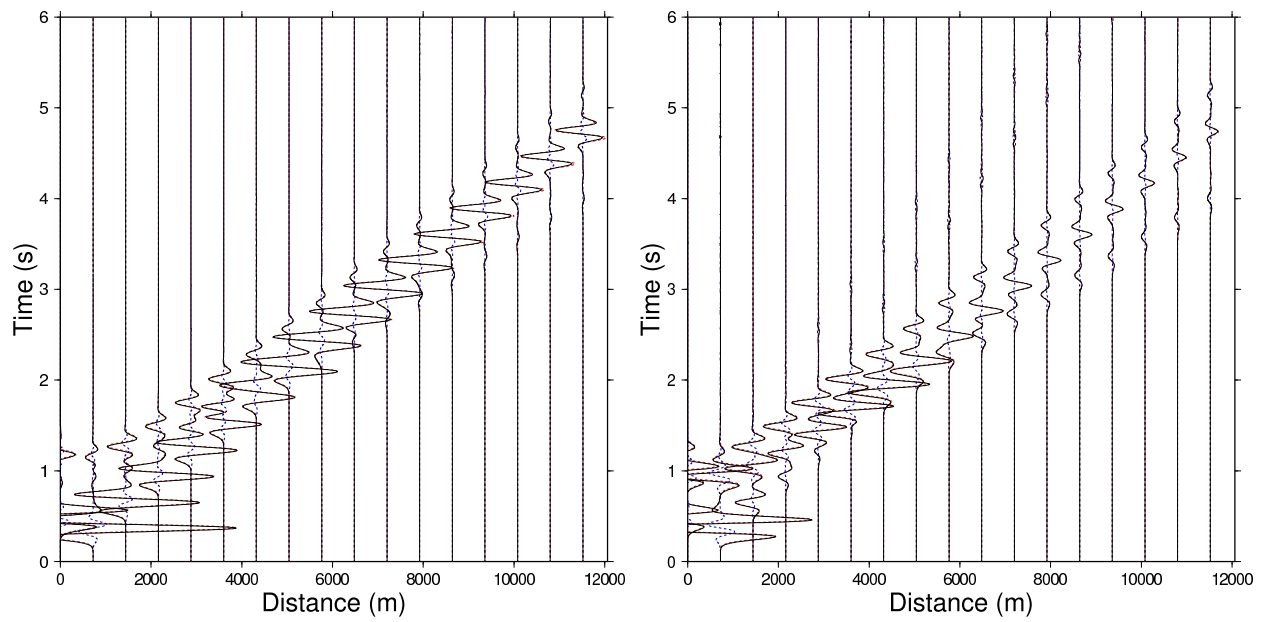


**Figure 11.** Seismograms computed for two elastic-layer model. Horizontal and vertical components of velocity at receivers are shown on the left and on the right respectively. Analytical solution is represented by discontinuous red lines, FV by continuous black lines and residuals by discontinuous blue lines.

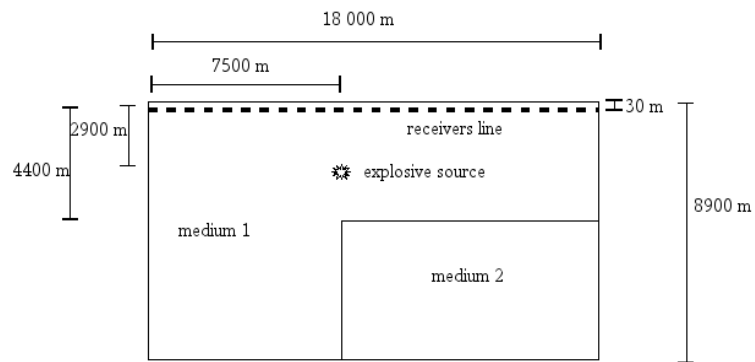


**Figure 12.** *Geometry of the Corner-Edge model.*

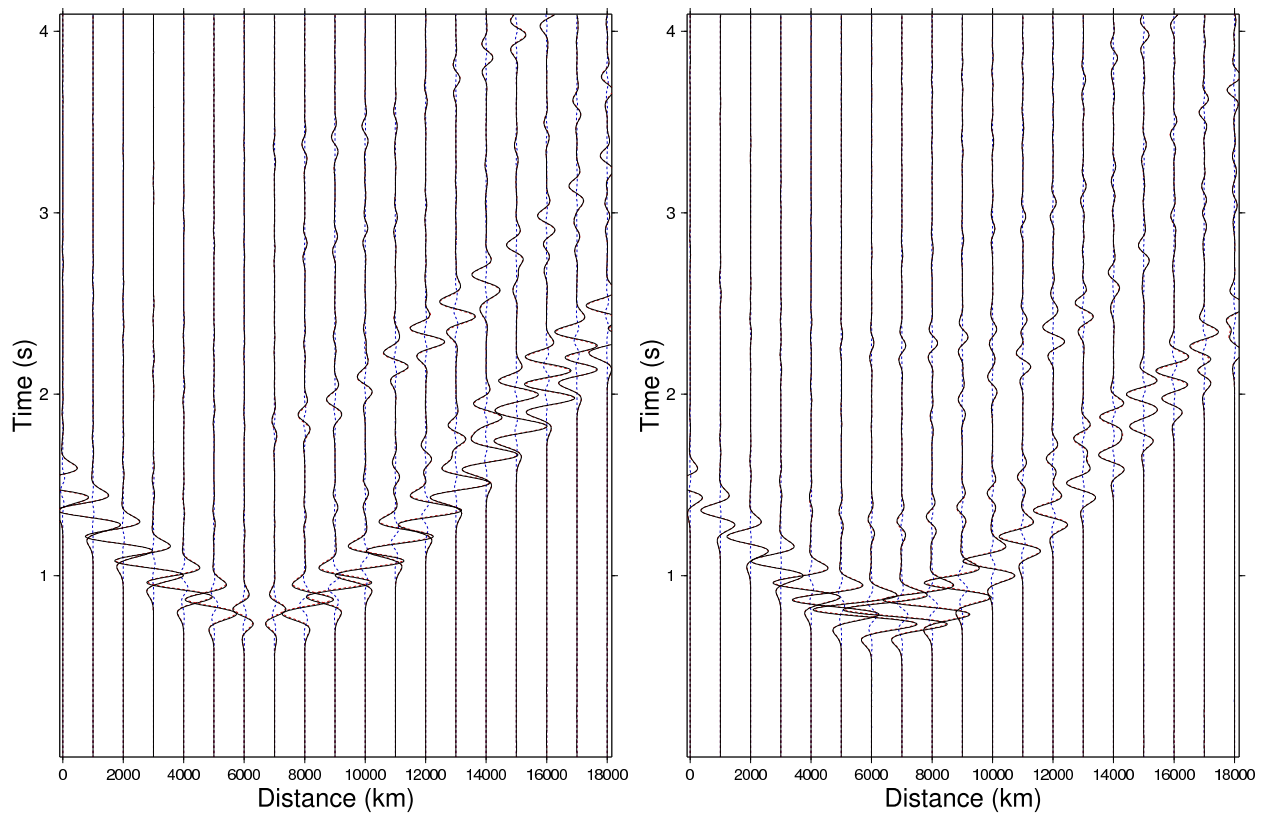


**Figure 13.** Seismograms computed in the Corner-Edge model. Horizontal and vertical components of velocity at receivers are shown on the left and on the right respectively. Reference solution computed with the FD method is represented by discontinuous red lines, FV by continuous black lines and residuals by discontinuous blue lines. Both solutions are very similar in the entire time window.

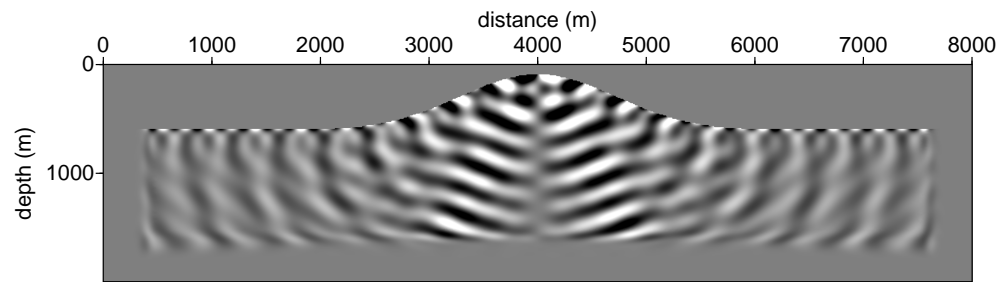


**Figure 14.** *Monochromatic wavefield of horizontal velocity in Hill model. Real part of wavefield is illustrated for a 10 Hz simulation*

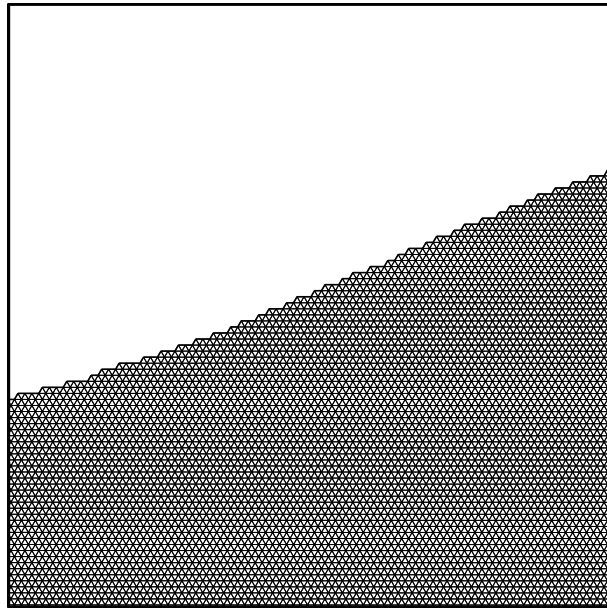


**Figure 15.** *Description of complex topography with regular equilateral triangles*

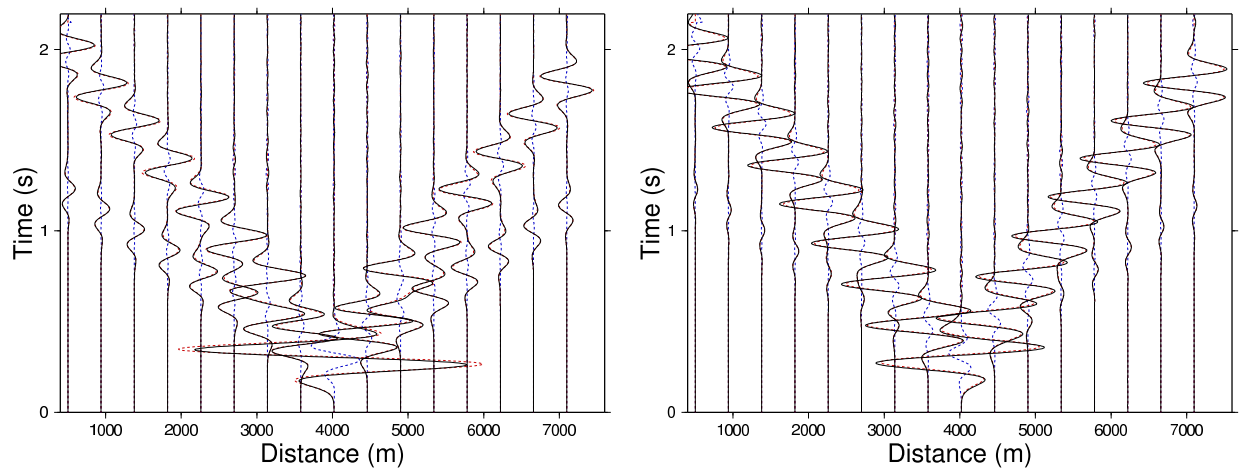


**Figure 16.** Seismograms computed in the hill model for the horizontal (left) and vertical (right) components of velocity. Reference solution computed with the FD method is represented by discontinuous red lines, the FV solution by continuous black lines and the difference between the two solutions with discontinuous blue lines.

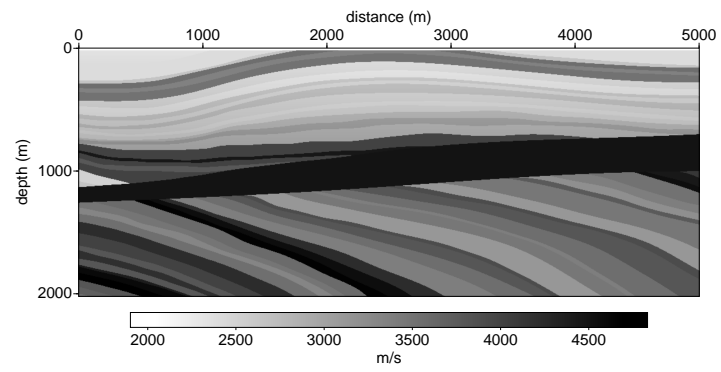


**Figure 17.** *P-wave velocity distribution of realistic model taken from the Marmousi 2 model.*



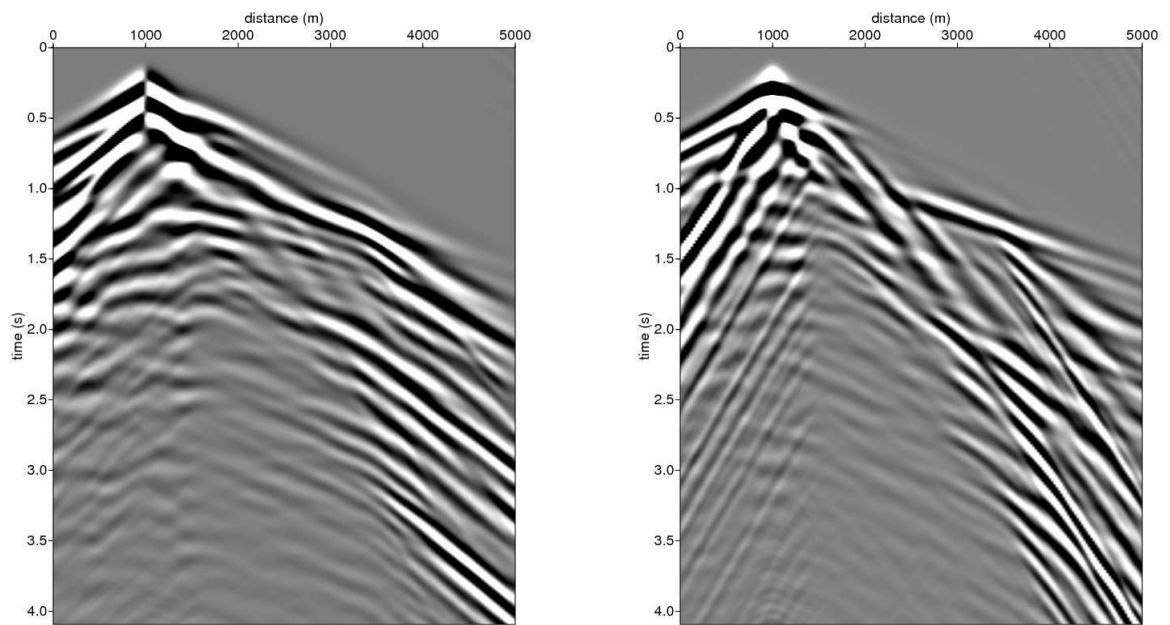


**Figure 18.** *Seismograms computed in the target of the Marmousi 2 model with the FV method using a regular equilateral mesh. Vertical and horizontal particle velocities at receiver positions are shown on the left and right respectively.*

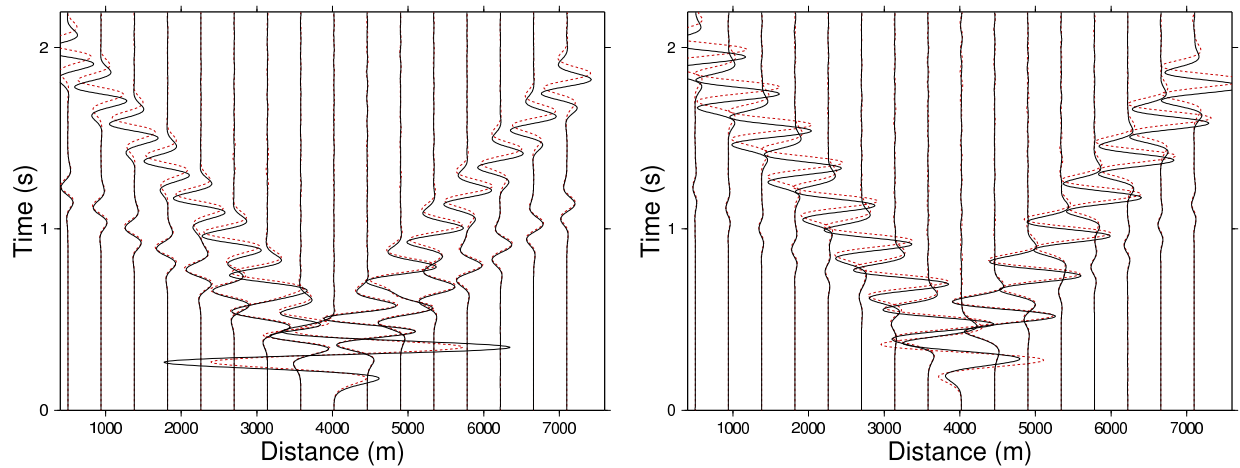


**Figure 19.** Seismograms computed in the hill model using equilateral and unstructured meshes. Horizontal and vertical components of particle velocity at receivers are on the left and right respectively. Reference solution computed with FV in regular equilateral mesh is plotted with discontinuous red lines and solution in unstructured mesh with continuous black lines. Note the advance of the solution computed in unstructured mesh increasing with propagation time.

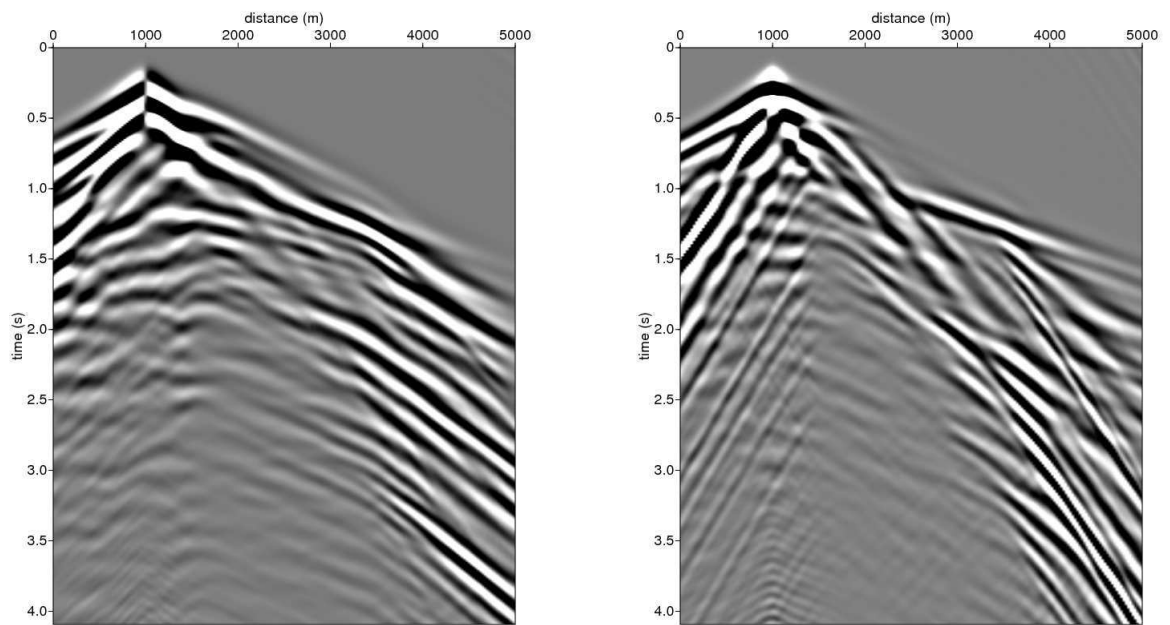


**Figure 20.** *Seismograms computed in the target of the Marmousi II model using unstructured mesh. Horizontal and vertical components of velocity at receivers are shown on the left and right respectively. These seismograms can be compared with that computed in the same model parameterized with an equilateral mesh (Figure 18).*

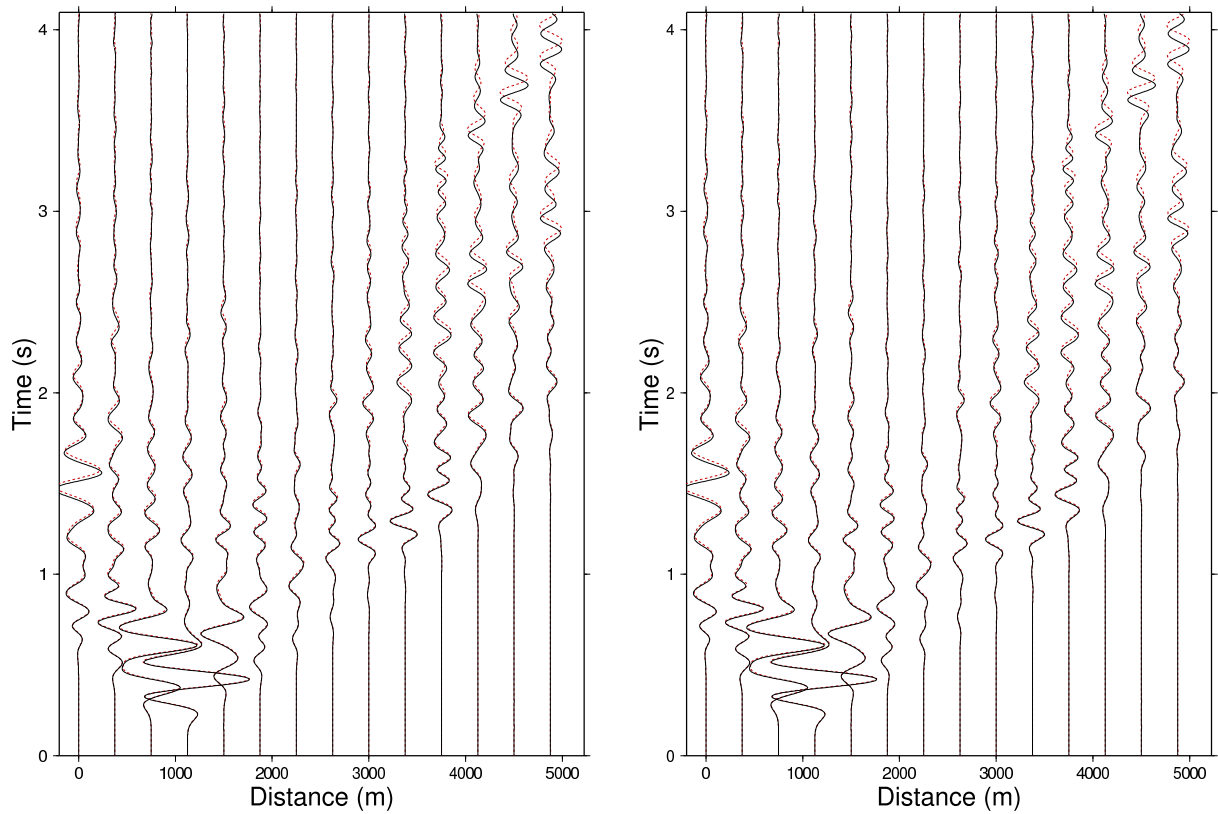


**Figure 21.** Comparison between FV seismograms computed in the target of the Marmousi II model with equilateral and unstructured meshes. Horizontal and vertical components of velocity at receivers are shown on left and right respectively. Reference solution computed with FV in regular equilateral mesh is represented by discontinuous red lines and solution in unstructured mesh by continuous black lines.

Numerical method	regular FV	unstructured FV	FD
Number of unknowns to solve	1 421 364	549 638	4 850 020
Time to prepare data for matrix building	54.4 s	40.1 s	1.0 s
Time for matrix building	1.6 s	0.80 s	10.9 s
Time for factorization	272.3 s	79.5 s	999.4 s
Memory use for factorization	3448 Mb	1333 Mb	12061 Mb
Time for resolution of 1 shot	3.8 s	1.7 s	13.5 s

**Table 1.** Comparison of numerical cost for the FV in regular and unstructured meshes and the FD methods in frequency domain for realistic model at 13 Hz.

**APPENDIX A: FINITE VOLUME DEVELOPMENT**

FV method is applied to first-order elastodynamic system described by equations 2. By introducing projector matrix  $M_x$ ,  $N_x$ ,  $M_z$  and  $N_z$  defined by :

$$\begin{aligned} N_x &= M_x^t = \begin{bmatrix} 1 & 1 & 0 \\ 0 & 0 & 1 \end{bmatrix} \\ N_z &= M_z^t = \begin{bmatrix} 0 & 0 & 1 \\ 1 & -1 & 0 \end{bmatrix} \end{aligned} \quad (\text{A1})$$

and diagonal matrix  $\Lambda = \text{diag}(\frac{1}{\lambda+\mu}, \frac{1}{\mu}, \frac{1}{\mu})$ , system 2 can be written in a vectorial form with a divergence expression:

$$\begin{aligned} -\omega\rho\vec{V} &= \overrightarrow{\text{div}(s_x N_x \vec{T}, s_z N_z \vec{T})} - \frac{\partial s_x N_x \vec{T}}{\partial x} - \frac{\partial s_z N_z \vec{T}}{\partial z} + \rho\vec{F} \\ -\omega\Lambda\vec{T} &= \overrightarrow{\text{div}(s'_x M_x \vec{V}, s'_z M_z \vec{V})} - \frac{\partial s'_x M_x \vec{V}}{\partial x} - \frac{\partial s'_z M_z \vec{V}}{\partial z} - \omega\Lambda\vec{T}^0 \end{aligned} \quad (\text{A2})$$

We introduce vectorial forms:  $\vec{G}(\vec{T}) = (s_x N_x \vec{T}, s_z N_z \vec{T})$  and  $\vec{H}(\vec{V}) = (s'_x M_x \vec{V}, s'_z M_z \vec{V})$ . We apply a surface integration over a control cell identified by the index  $i$ .

$$\begin{aligned} \int_{K_i} -\omega\rho\vec{V}dS &= \int_{K_i} \overrightarrow{\text{div}(\vec{G}(\vec{T}))}dS - \int_{K_i} \frac{\partial s_x N_x \vec{T}}{\partial x}dS - \int_{K_i} \frac{\partial s_z N_z \vec{T}}{\partial z}dS + \int_{K_i} \rho\vec{F}dS \\ \int_{K_i} -\omega\Lambda\vec{T}dS &= \int_{K_i} \overrightarrow{\text{div}(\vec{H}(\vec{V}))}dS - \int_{K_i} \frac{\partial s'_x M_x \vec{V}}{\partial x}dS - \int_{K_i} \frac{\partial s'_z M_z \vec{V}}{\partial z}dS - \int_{K_i} \omega\Lambda\vec{T}^0dS \end{aligned} \quad (\text{A3})$$

Thanks to Green theorem, surface integration of divergence terms let appear flux integrals:

$$\begin{aligned} \int_{K_i} -\omega\rho\vec{V}dS &= \int_{\partial K_i} \vec{G}(\vec{T})\vec{n}dL - \int_{K_i} \frac{\partial s_x N_x \vec{T}}{\partial x}dS - \int_{K_i} \frac{\partial s_z N_z \vec{T}}{\partial z}dS + \int_{K_i} \rho\vec{F}dS \\ \int_{K_i} -\omega\Lambda\vec{T}dS &= \int_{\partial K_i} \vec{H}(\vec{V})\vec{n}dL - \int_{K_i} \frac{\partial s'_x M_x \vec{V}}{\partial x}dS - \int_{K_i} \frac{\partial s'_z M_z \vec{V}}{\partial z}dS - \int_{K_i} \omega\Lambda\vec{T}^0dS \end{aligned} \quad (\text{A4})$$

where  $\partial K_i$  is boundaries of cell  $K_i$  and  $\vec{n}$  the external normal vector of  $\partial K_i$ .

We end up with the discrete system already explained written in a vectorial form. Partial derivatives of all PML functions are cancelled by  $P_0$  assumption.

$$\begin{aligned} -\omega A_i \rho_i \vec{V}_i &= \sum_{j \in \partial K_i} l_{ij} G_{ij} + A_i \rho_i \vec{F}_i \\ -\omega A_i \Lambda_i \vec{T}_i &= \sum_{j \in \partial K_i} l_{ij} H_{ij} - \omega A_i \Lambda_i \vec{T}_i^0 \end{aligned} \quad (\text{A5})$$

Integration of property 5 and flux formulation 4 in discret system A5 gives the 1<sup>st</sup> order discret system where parsimonious strategy can be applied:

$$\begin{aligned}
 \omega^2 \vec{V}_i &= \frac{\omega}{A_i \rho_i} \sum_{j \in \partial K_i} l_{ij} (n_{ijx} N_x s_{x_j} + n_{ijz} N_z s_{z_j}) \frac{\vec{T}_j}{2} + \omega \vec{F}_i \\
 \omega^2 \vec{T}_i &= \frac{\omega \Lambda_i^{-1}}{A_i} \sum_{j \in \partial K_i} l_{ij} (n_{ijx} M_x s'_{x_j} + n_{ijz} M_z s'_{z_j}) \frac{\vec{V}_j}{2} + \omega^2 \vec{T}_i^0
 \end{aligned} \tag{A6}$$